Research Square

Preprints are preliminary reports that have not undergone peer review.
They should not be considered conclusive, used to inform clinical practice,
or referenced by the media as validated information.

Direct integration of stretchable modules for implantable bioelectronics

Yesol Kim
Institute for Basic Science
Hoechang Chung
Institute for Basic Science
Chanhui Park
Institute for Basic Science
Seonghyeon Nam
Institute for Basic Science
Sung-Hyuk Sunwoo
Institute for Basic Science
Dae-Hyeong Kim
dkim98@snu.ac.kr

Institute for Basic Science

Article

Keywords:

Posted Date: November 12th, 2026

DOI: https://doi.org/10.21203/rs.3.rs-11293766/v1

License: This work is licensed under a Creative Commons Attribution 4.0 International License.
Read Full License

Additional Declarations: No competing interests reported.

Direct integration of stretchable modules for implantable bioelectronics

Yesol Kim[1,2⊥], Hoechang Chung[1,2⊥], Chanhui Park[1,2⊥], Seonghyeon Nam[1,2], Sung-Hyuk Sunwoo[1, 3]*, and Dae-Hyeong Kim[1,2]*

[1]*Center for Nanoparticle Research, Institute for Basic Science (IBS), Seoul 08826, Republic of Korea.*

[2]*School of Chemical and Biological Engineering, Institute of Chemical Processes, Seoul National University, Seoul 08826, Republic of Korea.*

[3]*Department of Chemical Engineering, Inha University, 100 Inha-ro, Michuhol-gu, Incheon 22212, Republic of Korea.*

[⊥]These authors equally contributed to this work.

*To whom correspondences should be addressed.

E-mail: shsunwoo@inha.ac.kr; dkim98@snu.ac.kr

Abstract

Stretchable implantable bioelectronics enable mechanically compliant operation on deforming tissues, yet system-level integration remains challenging. Integrating electrode, interconnect, and circuit modules often requires additional adhesive or conductive bonding layers at their junctions, complicating fabrication and potentially compromising mechanical robustness. Here, we introduce an interlayer-free integration strategy that combines self-healing polymer substrates with liquid metal conductors. Healing-mediated interfacial reconstruction of the polymer substrates forms mechanically cohesive junctions within minutes of contact, while fluidic reconnection of the liquid metal establishes electrical continuity between modules. These junctions exhibit an interfacial toughness of 600 N m^{-1} and maintain electrical continuity at tensile strains of approximately 1,000%. Electrode impedance and charge storage capacity show limited changes after repeated stretching. Self-healing between overlapping regions of the polymer substrate further secures electrodes wrapped around the heart and sciatic nerve. The assembled wireless systems deliver cardiac and sciatic nerve stimulation in rat models, demonstrating their stable operation in vivo. Together, these results extend self-healing beyond damage repair to system assembly and tissue fixation, enabling stretchable bioelectronics to function on dynamically moving organs.

Introduction

Stretchable implantable bioelectronics accommodate tissue deformation while maintaining conformal contact and reliable electrical function[1–4]. Recent advances in stretchable electronic components – electrodes, interconnects and circuits – have enabled bioelectronic systems to perform physiological recording[5,6], wound monitoring[7–9], cardiac pacing[10–15], neural modulation[16–18]. Partially stretchable systems combine stretchable electrodes and interconnects with rigid circuit modules[19–21], whereas monolithic stretchable systems fabricate these components as a single connected structure on a common substrate[2,11,17]. However, the constituent components have distinct material and fabrication requirements, making it difficult to optimize each of them within a shared fabrication process. Modular fabrication offers an alternative by allowing each component to be optimized independently before assembly into a complete system[19,22,23].

Despite these advantages, stretchable electronics assembled from modular components can suffer from limitations at the junctions between the modules[24–26]. Their assembly commonly relies on additional adhesive or conductive bonding layers to provide mechanical attachment, electrical connection, or both. These bonding layers constitute interlayers at the module junctions and can have mechanical properties that differ from those of the adjoining soft components[24–31], even when each module is stretchable (Fig. 1a). Such heterogeneous junctions can localize strain and promote interfacial failure under deformation, thereby limiting system-level reliability and durability[19,32–34]. Additional bonding layers also introduce extra processing steps and complicate the scalable assembly of complete systems. An ideal integration strategy should therefore enable the constituent modules themselves to form mechanically robust and electrically continuous junctions without additional interlayers while preserving system-level stretchability.

Self-healing materials enable the formation of module junctions through the substrate itself. In dynamic polymer networks, reversible interactions reform across damaged surfaces, restoring mechanical integrity after fracture[35–39]. Beyond this conventional role, the same interfacial reconstruction can be initiated during assembly, allowing separately fabricated substrates to develop mechanical cohesion upon contact[40–42]. The substrate can therefore provide both structural support for each module and mechanical bonding between modules. For this approach to support functional system integration, conductive pathways must also be established across the assembled interface. Liquid metals provide an electrical counterpart: their fluidity allows conductors in separately fabricated modules to merge upon contact, establishing an electrically continuous pathway across the junction[43,44]. Redistribution of the liquid metal within deforming conductor structures can compensate for strain-induced geometric changes, enabling strain-resilient electrical performance[13,45–49].

Here, we establish an interlayer-free integration strategy for modular stretchable implantable bioelectronics by combining self-healing polymer substrates with liquid metal conductors. During assembly, the self-healing polymer substrates of adjacent modules form a mechanically cohesive junction, while the liquid metal conductors merge to provide electrical continuity. This allows electrode, interconnect and wireless circuit modules to be fabricated separately and assembled without additional adhesive or conductive bonding layers (Fig. 1b). The junctions remain mechanically and electrically functional under deformation, while the assembled system maintains its wireless powering capability. The polymer substrates further enable self-wrapping interfaces with the heart and sciatic nerve, through self-healing between overlapping substrate regions. We demonstrate the integrated systems through physiological recording and wireless cardiac and sciatic nerve stimulation in rat models. Together, these results establish a strategy for assembling independently fabricated stretchable modules into

complete implantable systems without additional interlayers.

Results

System architecture and mechanism of modular assembly

The implantable system comprises independently fabricated electrode, interconnect and wireless circuit modules, each designed to preserve a distinct function during deformation (Fig. 1c). The electrode module provides a strain-resilient electrochemical interface with tissue, the interconnect maintains electrical conduction pathways at junctions and the circuit module shows strain-resilient wireless power transfer performance. Integrating these modules follows an align-press-heal sequence (Fig. 1d). The liquid metal (LM) conductor patterns are first aligned, and the adjoining modules are then pressed together. During contact, the fluidic LM conductors reconnect to establish an electrical pathway, while interfacial chain reconstruction between the self-healing polymer (SHP) substrates forms a mechanically cohesive junction around them. Together, these processes establish electrical and mechanical connections without an additional bonding interlayer. Sequential face-to-face assembly joined the electrode and wireless circuit modules through the interconnect to produce the complete implantable system (Fig. 1e). For in vivo operation, we integrate a wireless power transfer system with the device, and the circuit was positioned subcutaneously, while the electrode was placed at the cardiac or sciatic nerve interface (Fig. 1f). The SHP substrate was wrapped around the tissue so that overlapping regions attached to one another, providing a conformal, mechanically anchored electrode interface during dynamic tissue motion (Fig. 1g).

Interlayer-free integration of stretchable modular bioelectronics

Figure 2a summarizes the fabrication and integration process for stretchable bioelectronic

modules (Supplementary Fig. 1). The process combines SBS-enabled high-resolution LM patterning (Supplementary Figs. 2 and 3) with module-specific fabrication procedures (Supplementary Figs. 4 and 5), followed by interlayer-free assembly (Supplementary Video 1).

First, a SHP substrate (400 μm) was spin-coated onto a sacrificial parylene layer. Then an SBS processing layer was coated onto the SHP substrate, followed by Cr/Cu deposition (5 nm/80 nm) and photopatterning to define the metal traces. Liquid metal was subsequently applied to wet the patterned traces, and the SBS processing layer was selectively removed from the junction regions by dry etching to expose the SHP surface. An SHP encapsulation layer was then transferred onto the device, leaving the junction regions accessible for assembly. After release from the Si wafer, the sacrificial parylene layer was removed by dry etching. Finally, the separately fabricated modules were aligned at their junctions and pressed together, allowing the SHP surfaces to heal across the interface and the liquid metal conductors to reconnect.

The resulting junctions accommodated deformation without additional adhesive or conductive bonding layers. Compared with junctions formed using commercial epoxy resin or carbon tape, the direct SHP interface accommodated substantially larger deformation and maintained electrical connectivity at tensile strains of approximately 1,000% (Fig. 2b and Supplementary Figs. 6–13). Beyond the mechanical compliance of the bonding interface, the conductor traces also determined whether electrical connections between modules could withstand deformation. A comparison of Cr/Cu, a liquid metal particle (LMP) composite and fluidic LM showed that Cr/Cu rapidly lost electrical continuity upon stretching, whereas the LMP composite tolerated greater strain but eventually exhibited an abrupt increase in resistance. LM, in contrast, showed a smaller resistance change and maintained electrical continuity throughout the tested strain range, consistent with its ability to flow and reconfigure as the junction deformed (Fig. 2c and Supplementary Figs. 14 and 15). These comparisons support

the combined use of SHP substrates and LM conductors to form deformation-tolerant module junctions.

The stability of the assembled junctions was evaluated during incubation in PBS at 37 °C (Supplementary Fig. 16). Ga release was quantified using inductively coupled plasma mass spectrometry (ICP–MS), with measured concentrations remaining below 0.1 ppm over 14 days (Fig. 2d). Separately, direct cutting and rejoining of the SHP demonstrated rapid interfacial reconstruction at room temperature. After 10 min of contact, the healed sample sustained large deformation (Fig. 2e). During PBS incubation, the shear strength of the reconstructed interface showed no statistically significant differences across incubation times up to 28 days (Fig. 2f). The fully integrated device also exhibited limited swelling over the 28-day incubation period (Fig. 2g and Supplementary Fig. 17).

Strain-resilient electrochemical performance of Pt-LMP composite electrodes

To accommodate tissue deformation while providing an electrochemically functional interface, we developed a Pt-LMP composite electrode combining deformable liquid metal particles with Pt black[50,51]. The composite successfully encapsulated fluidic LM at the exposed electrode sites (Fig. 3a)[48,52]. LM droplets were first broken down into microparticles by tip sonication. The resulting LMPs were then thoroughly mixed with Pt black microparticles in a styrene–ethylene–butylene–styrene (SEBS) solution to form a homogeneous composite dispersion. Upon stretching, the deformable LMPs can reorganize to maintain conductive pathways[13,32,46], while the dispersed Pt black provides electrochemically active sites. Scanning electron microscopy (SEM) and energy-dispersive X-ray spectroscopy (EDS) analyses confirmed the distribution of LMPs and Pt black within the polymer matrix (Fig. 3b).

Increasing the Pt black loading progressively reduced the electrode impedance, with the Pt-LMP composite exhibiting an approximately 36% lower impedance at 1 kHz than the Pt-black-free composite (Fig. 3c). The charge storage capacity (CSC) and injected charge density also increased with Pt black loading (Fig. 3d and Supplementary Fig. 18), demonstrating enhanced charge-storage and charge-injection characteristics. The composite also maintained electrical conduction over a broad strain range (Fig. 3e) and showed a modest resistance increase during 1,000 stretching cycles at 50% strain (Fig. 3f). After repeated stretching cycles, its impedance increased by approximately 14%, compared with approximately 122% for the AgNW composite control (Fig. 3g, h and Supplementary Figs. 19 and 20). Cyclic voltammetry and biphasic-pulse measurements further showed limited changes in electrochemical performance after repeated stretching (Fig. 3i, j and Supplementary Fig. 21).

Wireless power transfer and circuit operation under strain

To translate the strain-resilient electrode interface into an operating implantable system, we integrated a wireless circuit module to provide stable power delivery and controlled stimulation. Figure 4a illustrates the wearable-to-implant wireless power transfer system and the block diagram of the implanted device. The power management circuit comprises a receiver coil, a Schottky-diode rectifier and a low-dropout linear regulator (LDO). The Schottky diode converts the received AC signal into DC with a low forward-voltage drop, while the LDO supplies a regulated voltage to the microcontroller (MCU). For cardiac stimulation, four stimulation electrodes and one common ground electrode are connected to the MCU, with two stimulation electrodes positioned on each ventricle. For nerve stimulation, a single stimulation electrode and a ground electrode are used. The separately fabricated electrode, interconnect

and wireless circuit modules were assembled into a complete system, which maintained wirelessly powered LED operation at 0% and 30% strain (Fig. 4b and Supplementary Fig. 22).

The strain-resilient conductivity of the LM enables the stretchable implanted device to maintain robust wireless power transfer performance under biaxial strains of up to 30%. The normalized quality factor (Q factor) decreased by approximately 19.0% at 30% strain (Fig. 4c), while S_{11} spectra revealed an approximately 4.9% decrease in resonant frequency from 2.24 MHz at 0% strain to 2.13 MHz at 30% strain (Fig. 4d). The rectified voltage and transferred power showed no substantial degradation at 30% strain relative to the unstrained state across the tested load range (0-300 Ω) (Fig. 4e). Transferred power peaked at a load resistance of approximately 50-80 Ω, comparable to the effective load of the integrated electronic components, supporting power delivery near the device operating load. The voltage gains also remained comparable between the two strain conditions (0% and 30%) over transmission distances of 0-5 mm (Fig. 4f)[53].

Figure 4g presents representative voltage waveforms measured at successive stages of the wireless power transfer system under 0% and 30% strain, from the wearable transmitter to the receiver circuit and MCU output. Considering that the physiological strain of the heart generally remains below 30%, the waveforms were characterized under 0% and 30% strain. Owing to the strain tolerance, comparable received and rectified voltages were obtained under both strain conditions and the MCU consequently generated a stable stimulation waveform at 40 Hz with a 60% duty cycle, regardless of the applied strain. Voltage levels measured at each stage further confirmed that the stimulation output remained stable despite variations in the received voltage (Fig. 4h). Together, these results demonstrate that the assembled system maintains wireless powering and controlled stimulation under mechanical deformation.

Wireless cardiac and peripheral nerve stimulation in rats

The integrated bioelectronic system was evaluated in vivo for wireless cardiac and peripheral nerve stimulation. To establish the cardiac interface, the electrode module was positioned on the epicardial surface, and the extensions of the SHP substrates were wrapped around the heart and joined through self-healing (Fig. 5a). This configuration secured the electrode array without additional adhesives or rigid fixation structures and maintained conformal contact with the myocardium during cardiac motion. The wireless circuit module was implanted subcutaneously in the abdominal region to receive power from the external transmitter and deliver stimulation through the integrated electrode modules (Fig. 5b).

We first compared the electrophysiological recording and cardiac stimulation performance of Pt-LMP composite and LM electrodes. The Pt-LMP electrodes recorded epicardial electrograms with a higher signal-to-noise ratio (SNR) than the LM electrodes (Fig. 5c). Strength-duration analysis also showed that the Pt-LMP electrodes consistently exhibited lower stimulation threshold voltages across the measured pulse-duration range (Fig. 5d). These findings are consistent with the electrochemical characteristics described above and demonstrate the suitability of the Pt-LMP composite for both electrophysiological recording and electrical stimulation at the tissue interface.

We next evaluated the integrated system for wireless cardiac pacing at 360 bpm (6 Hz). Activation of the transmitter induced cardiac electrical responses synchronized with the stimulation pulses (Fig. 5e). The R-R interval shortened during pacing and returned toward its pre-pacing level after the transmitter was switched off (Fig. 5f). The QT interval was also shorter during pacing than at baseline (Fig. 5g).

The system was further evaluated under bradycardic conditions, in which the R-R interval was prolonged to 948 ms (Fig. 5h). Surface electrocardiogram (ECG) recordings showed an

increase in the ventricular activation rate during wireless stimulation relative to the bradycardic baseline (Supplementary Fig. 23). Following cessation of pacing, spontaneous sinus rhythm was observed with an R-R interval of 228.9 ms.

The self-healing fixation strategy was further extended to the peripheral nerve interfaces. The electrode module was wrapped around the exposed sciatic nerve, and the SHP extensions were joined through self-healing to secure the module in conformal contact with the nerve surface (Fig. 5i, j). Wireless stimulation at 3 V induced lower-limb movement with an angular displacement of approximately 38° (Fig. 5k). This motor response demonstrates functional neuromuscular activation through the implanted electrode interface and supports the applicability of the modular system to both cardiac and peripheral nerve stimulation.

Discussion

This study presents an interlayer-free integration strategy for stretchable implantable bioelectronics in which the constituent materials themselves form the modular junctions. Interfacial reconstruction of the SHP substrates provides mechanical cohesion, while fluidic merging of LM conductors establishes electrical continuity across module junctions. This complementary material design separates component fabrication from system assembly, allowing electrode electrochemistry, interconnect conduction under strain, and circuit functions for wireless powering and stimulation to be optimized independently. These distinct requirements can therefore be addressed without a shared monolithic fabrication process or additional adhesive or conductive bonding layers. The resulting junctions maintain mechanical integrity and electrical continuity under deformation, preserving the function of the assembled system.

The same self-healing substrates also extend this integration principle to tissue fixation.

Integrating overlapping substrate regions after wrapping around the heart or sciatic nerve secures conformal electrode interfaces without a separate tissue adhesive layer or rigid fixation structure. Cardiac and peripheral nerve demonstrations show that this wrapping strategy supports wireless stimulation on dynamically moving tissues. Independent module fabrication further provides a basis for adapting device geometries and functions to different anatomical and physiological requirements. Chronic implantation studies will be needed to establish long-term mechanical stability and biocompatibility. Together, these findings show how self-healing substrates and fluidic conductors can bridge independently fabricated components, functional systems, and moving tissues through the constituent materials themselves.

Methods

Materials

Poly(tetramethylene ether) glycol (PTMEG, Mn = 1,000) and isophorone diisocyanate (IPDI) were purchased from Tokyo Chemical Industry (TCI). Dibutyltin dilaurate (DBTDL) was purchased from Sigma-Aldrich. N,N-Dimethylacetamide (DMAc) was purchased from Samchun Chemical, and bis(4-hydroxyphenyl) disulfide was purchased from 3A Senrise. TUFTEC™ H1062 poly(styrene-ethylene-butylene-styrene) (SEBS) was obtained from Asahi Kasei, and KTR101 poly(styrene-butadiene-styrene) (SBS) was obtained from Kumho Chemicals. Eutectic gallium–indium (EGaIn; 75.5 wt% Ga and 24.5 wt% In) was used as the liquid metal. Pt black powder (≤20 μm) was purchased from Sigma-Aldrich. Dragon Skin 20 and Ecoflex 00-50 were obtained from Smooth-On. VHB tape (3M), epoxy resin (V-tech), and carbon tape (Seongho Sigma) were used as representative bonding materials.

Synthesis of the self-healing polymer

PTMEG (Mn = 1,000; 4.83 g) was dehydrated under vacuum at 100 °C for 1 h and transferred to a glovebox, where all subsequent synthesis steps were performed. The PTMEG was equilibrated at 70 °C, after which IPDI (2.2567 g, 2.13 mL) and DBTDL (0.0167 g, 15.6 μL), dissolved in DMAc (1.67 mL), were added. The reaction mixture was stirred at 70 °C for 2 h and then cooled to room temperature. Bis(4-hydroxyphenyl) disulfide (1.21 g) was dissolved in DMAc (3.33 mL), added to the reaction mixture, and stirred at 40 °C for 1.5 h. The resulting SHP solution was finally degassed under vacuum for 1 h to remove residual air.

Preparation of Pt-LMP composite

SEBS (TUFTEC™ H1062) was dissolved in toluene at 90 mg mL^{-1}. EGaIn (700 mg) was added to SEBS solution (2 mL) and tip-sonicated at 70% amplitude for 30 min using a 3 s on/1 s off pulse sequence to form liquid-metal particles (LMPs). Pt black powder (0, 50, or 100 mg) was subsequently added, followed by vortex mixing for approximately 1 min. The resulting Pt-LMP–SEBS dispersion was drop-casted onto the target substrate and thermally dried at 65 °C for 5 min.

Fabrication of stretchable electrode and interconnect modules

Stretchable electrode and interconnect modules were fabricated on Si or glass wafers coated with either a parylene sacrificial layer or a Au sacrificial layer (10 nm). The SHP solution was spin-coated at 150 rpm and thermally treated for 12 h while the temperature was gradually increased from 40 to 130 °C, followed by post-treatment in a vacuum oven at 60 °C for 6 h. The SHP surface was treated by O_2 reactive-ion etching (RIE; 0.1 sccm, 30 W, 2 min), followed by spin-coating of SBS in toluene (30 mg mL^{-1}) at 1,000 rpm. The SBS processing layer was introduced to stabilize the SHP during subsequent solvent and thermal processing and to

support reliable metal patterning. After a second O_2 RIE treatment under the same conditions, Cr/Cu traces (5 nm/80 nm) were deposited by electron-beam evaporation and patterned using either a shadow mask or AZ 5214-based photolithography. EGaIn was treated with 0.1 M HCl before selective wetting onto the patterned Cr/Cu traces. The exposed SBS was subsequently removed by O_2 RIE (0.1 sccm, 150 W, 2 min 30 s), with the patterned metal traces serving as an etch mask, to expose the underlying SHP at regions designated for module integration. A laser-cut SHP encapsulation film was then aligned and gently pressed onto the exposed SHP surface without an additional adhesive layer.

Fabrication of stretchable circuit modules

Stretchable circuit modules were fabricated on SHP using the same procedure described above for the first conductive layer. Junction areas were protected with removable PDMS masks. Dragon Skin 20 was spin-coated at 500 rpm and cured at 65 °C for 2 h to form the dielectric layer. After O_2 RIE treatment (0.1 sccm, 30 W, 2 min), vertical interconnection access (VIA) openings were laser-patterned through the Dragon Skin dielectric to expose the first LM layer. A second Cr/Cu layer (5 nm/80 nm) was then deposited and patterned, followed by LM wetting to form the second conductive layer and establish electrical connection with the first LM layer through the VIA openings. Electronic components were directly positioned onto the LM-patterned contact regions without commercial solder, or conductive paste. The assembled circuit was encapsulated with Ecoflex 00-50 to mechanically secure the components, after which the PDMS masks were removed to expose the predefined junctions.

Mechanical characterization of the self-healing polymer and interfaces

Mechanical properties of the SHP and its bonded interfaces were characterized using a universal testing machine (Instron 34SC-1). For uniaxial tensile testing, rectangular SHP specimens (10 mm × 20 mm) were stretched at a crosshead speed of 100 mm min^{-1}. Young's modulus was determined from the initial linear region of the stress–strain curve. Lap-shear strength was measured based on ASTM F2255. Two SHP specimens (10 mm × 20 mm) were overlapped over a 10 mm × 10 mm area and compressed with a 200 g weight for 2 min or 10 min. Lap-shear testing was performed at 10 mm min^{-1}, and shear strength was calculated by normalizing the maximum force by the bonded area. Interfacial toughness was evaluated by 180° peel testing based on ASTM F2256. Specimens were bonded using the same procedure and peeled at 10 mm min^{-1}. Interfacial toughness was determined from the steady-state peel force, excluding the initial peak and terminal edge regions, and normalized by the specimen width.

Electromechanical characterization of stretchable conductors and self-healed interconnects

Electrical resistance was monitored during uniaxial tensile deformation using a B1500A Semiconductor Device Analyzer (Keysight Technologies) and a tensile stage (Jeil Optical Systems, Korea). Unless otherwise specified, specimens were 10 mm × 15 mm and were mounted on VHB tape when additional support was required. Tensile deformation was applied at a strain rate of 10% s^{-1}.

For Pt-LMP electrodes, the electrical response was expressed as the relative resistance change, $\Delta R/R_0$, where $\Delta R = R - R_0$. Resistance was measured during monotonic stretching and during 1,000 stretching cycles at 50% strain. To compare the electrical stability of different conductors across self-healed junctions, 2-mm-wide Cr/Cu, LMP composite, and LM traces were

fabricated on SHP substrates. The specimens were cut in half and rejoined with an overlap region 10 mm wide × 2 mm long, with the 2-mm-wide conductive traces aligned across the junction. The SHP interfaces were maintained in contact for 10 min before tensile testing, and resistance was monitored as a function of strain.

To evaluate the influence of the bonding interface on interconnect stretchability, identical LM interconnects were joined using direct SHP self-healing, carbon tape, or epoxy resin using the same junction geometry (overlap region, 10 mm wide × 2 mm long; conductive trace width, 2 mm). The samples were subjected to the same uniaxial tensile testing, and mechanical and electrical failure strains were determined for each bonding configuration.

Electrochemical characterization of stretchable electrodes

Electrochemical measurements were performed in 1× phosphate-buffered saline (PBS) using a CHI660E electrochemical workstation (CH Instruments) in a three-electrode configuration. The stretchable electrode, Ag/AgCl electrode, and Pt plate served as the working, reference, and counter electrodes, respectively. The exposed working-electrode area was 1 cm^2.

Electrochemical impedance spectroscopy (EIS) was performed from 0.1 Hz to 100 kHz using a 5 mV sinusoidal perturbation. Cyclic voltammetry (CV) was conducted from −0.9 to 0.1 V versus Ag/AgCl at 0.1 V s^{-1}. Charge storage capacity (CSC) was calculated by integrating the current density over the complete CV cycle and normalizing by the scan rate.

$$CSC\ (mC\ cm^{-2}) = \int_{V_2}^{V_1} \frac{j}{2v} dV$$

where j is the measured current density and v is the scan rate. The integration was performed over both the forward and reverse scans of the complete CV loop.

Injected charge density was evaluated by chronoamperometry using biphasic voltage pulses of ±0.5 V with a duration of 100 ms per phase. The charge density of each phase was obtained by

integrating the corresponding current–time response, and injected charge density was calculated as the sum of the cathodal and anodal charge densities.

$$Injected\ charge\ density\ (mC\ cm^{-2}) = \sigma_c + \sigma_a$$

where σ_c and σ_a represent the injected charge densities during the cathodal and anodal phases, respectively.

Receiver antenna characterization

The S_{11} magnitude of the receiver coil was measured using a vector network analyzer (Agilent Technologies, E5071C) while the coil was biaxially stretched from 0% to 30 % in 10% increments using a custom two-dimensional stretcher (NAMIL, NMC-201N). Owing to the limited resonance depth of the S_{11} response, the Q factor was estimated using the full width at half depth (FWHD) method. The calculated Q factor was normalized to its initial value, reported as Q/Q_0.

Power harvesting characterization

The received voltage and harvested power as a function of load resistance were measured at the output of the rectification circuit, consisting of an RB751S40 Schottky diode and a 10-uF smoothing capacitor, across resistive loads ranging from 10 Ω to 300 Ω. The separation between the transmitter and receiver coils was maintained at 1 mm.

To evaluate power transfer performance at different coil separations, the distance between the transmitter and receiver coils was varied using a custom-built jig. The voltage gain was calculated as the ratio of the receiver-to-transmitter peak-to-peak voltages, using an oscilloscope (Keysight, DSOX2002A). Voltage waveforms at individual circuit stages were

also recorded using an oscilloscope and a digital multimeter (Fluke 115) during wireless power transfer to the implanted device.

In vivo demonstration

All animal experiments were conducted in accordance with the guidelines of the Institutional Animal Care and Use Committee (IACUC) of Seoul National University (approval no. SNU-250614-1-1). Eight-week-old male rats purchased from Orient Bio (Republic of Korea) were acclimated for one week before experiments. Rats were anesthetized with 3% isoflurane, and the thoracic region was shaved and disinfected with 70% ethanol and povidone–iodine. The thoracic cavity was opened by midline thoracotomy, and the device was implanted as described in the main text. Epicardial electrograms were recorded using a conventional data acquisition system (PowerLab, ADInstruments, New Zealand). For wireless cardiac stimulation, the abdominal skin was dissected, and the wireless receiver was implanted subcutaneously. The transmitter was positioned above the receiver to deliver wireless electrical stimulation, and the resulting changes in cardiac rhythm were recorded.

For sciatic nerve stimulation, the skin over the medial thigh was incised using iris scissors, and the overlying muscle was carefully separated with forceps to expose the sciatic nerve. The SHP-based electrode was wrapped around the nerve and mechanically secured through adhesion between the SHP interfaces. Electrical stimulation was applied at amplitudes of 3 V, and the resulting movements of the rat hindlimb were recorded.

Statistical analysis

All error bars represent the standard deviation (n = 3). The data in Fig. 2f were analyzed using one-way analysis of variance (ANOVA; $p = 0.842$, $n = 3$). All data were processed using OriginLab.

Data availability

Data is provided within the manuscript or Supplementary information files.

Acknowledgements

This work was supported by the Institute for Basic Science (No. IBS-R006-A1); and funded by the Ministry of Science and ICT (MSIT) (No. RS-2025-00555824) and Ministry of Health and Welfare (RS-2025-02263839).

Author contributions

Y.K., H.C. and C.P. contributed equally to this work. Y.K., H.C. and C.P. conceptualized the study and designed the overall research. Y.K. and H.C. designed and fabricated the complete device system. Y.K. and C.P. conducted the wireless power transfer (WPT) experiments and analyzed system performance. Y.K., C.P. and S.-H.S. performed the in vivo experiments in rats and analyzed the physiological data. All authors discussed the results. Y.K., H.C., C.P. and S.-H.S. wrote the original draft, and S.N. and D.-H.K. reviewed and edited the manuscript. S.-H.S. and D.-H.K. supervised the project and secured funding.

Competing interests

The authors have no conflicts to disclose.

References

1. Mou, L., Xia, Y. & Jiang, X. Liquid metal-polymer conductor-based wireless, battery-free epidermal patch. *Biosens. Bioelectron.* **197**, 113765 (2022).

2. Xu, Y. *et al.* Phase-separated porous nanocomposite with ultralow percolation threshold for wireless bioelectronics. *Nature Nanotechnol.* **19**, 1158–1167 (2024).

3. Yamagishi, K., Lee, S., Yokota, T. & Someya, T. Soft, Flexible, and Stretchable Platforms for Tissue-Interfaced Bioelectronics. *Adv.Sci.* **13**, e21521 (2026).

4. Kim, H. J., Koo, J. H., Lee, S., Hyeon, T. & Kim, D. H. Materials design and integration strategies for soft bioelectronics in digital healthcare. *Nat. Rev. Mater.* **10**, 654–673 (2025).

5. Choi, S. *et al.* Highly conductive, stretchable and biocompatible Ag–Au core–sheath nanowire composite for wearable and implantable bioelectronics. *Nature Nanotechnol.* **13**, 1048–1056 (2018).

6. Lim, C. *et al.* Highly Conductive and Stretchable Hydrogel Nanocomposite Using Whiskered Gold Nanosheets for Soft Bioelectronics. *Adv. Mater.* **36**, 2407931 (2024).

7. Kim, Y., Park, C., Cha, G. D., Sunwoo, S. H. & Kim, D. H. Multifunctional microfluidic bioelectronic suture for accelerated healing and wound monitoring. *Lab Chip* **25**, 6582–6592 (2025).

8. Sani, E. S. *et al.* A stretchable wireless wearable bioelectronic system for multiplexed monitoring and combination treatment of infected chronic wounds. *Sci. Adv.* **9**, eadf7388 (2023).

9. Su, R. *et al.* A highly stretchable smart dressing for wound infection monitoring and treatment. *Mater. Today Bio* **26**, 101107 (2024).

10. Sunwoo, S. H. *et al.* Ventricular tachyarrhythmia treatment and prevention by subthreshold stimulation with stretchable epicardial multichannel electrode array. *Sci. Adv.* **9**, eadf7388 (2023).

11. Nam, S. *et al.* A wearable-to-implant wireless power transfer technology with variation tolerance. *Nat. Electron.;* 10.1038/s41928-026-01714-0 (2026).

12. Nam, S. *et al.* Needle-Like Multifunctional Biphasic Microfiber for Minimally Invasive Implantable Bioelectronics. *Adv. Mater.* **36**, 2404101 (2024).

13. Choi, H. *et al.* Adhesive bioelectronics for sutureless epicardial interfacing. *Nat. Electron.* **6**, 779–789 (2023).

14. Han, S. I. *et al.* Next-Generation Cardiac Interfacing Technologies Using Nanomaterial-Based Soft Bioelectronics. *ACS Nano* **18**, 12025–12048 (2024).

15. Park, C. *et al.* Liquid metal-based stretchable bioelectronic fiber for electrical stimulation and drug delivery in minimally invasive cardiac therapy. *APL Bioeng.* **9**, 026118 (2025).

16. Hong, G. & Lieber, C. M. Novel electrode technologies for neural recordings. *Nat. Rev. Neurosci.* **20**, 330–345 (2019).

17. Hui, Y. *et al.* Three-dimensional printing of soft hydrogel electronics. *Nat. Electron.* **5**, 893–

903 (2022).

18. An, S. *et al.* Self-Bondable and Strain-Durable Electroceuticals Using Self-Healing and Stretchable Conducting Nanocomposite Trilayer for Effective Vagus Nerve Stimulation. *ACS Nano* **19**, 33091–33102 (2025).

19. Jiang, Y. *et al.* A universal interface for plug-and-play assembly of stretchable devices. *Nature* **614**, 456–462 (2023).

20. Chang, Z. *et al.* Fully Implantable Wireless Cardiac Pacing and Sensing System Integrated with Hydrogel Electrodes. *Adv. Sci.* **11**, 2401982 (2024).

21. Song, J. W. *et al.* Bioresorbable, wireless, and battery-free system for electrotherapy and impedance sensing at wound sites. *Sci. Adv.* **9**, eade4687 (2023).

22. Wu, P. *et al.* A three-dimensional stretchable core–shell cable for soft and hybrid electronics that is patternable, recyclable and noise-resistant. *Nat. Electron.* **9**, 519–531 (2026).

23. Lee, S. *et al.* A body-scale textile-based electromyogram monitoring system with coaxially shielded conductive yarns. *Sci. Adv.* **11**, eadx4518 (2025).

24. Liu, Z., Valvo, P. S., Huang, Y. & Yin, Z. Cohesive failure analysis of an array of IC chips bonded to a stretched substrate. *Int. J. Solids Struct.* **50**, 3528–3538 (2013).

25. Sun, J. Y. *et al.* Debonding and fracture of ceramic islands on polymer substrates. *J. Appl. Phys.* **111**, 013517 (2012).

26. Gul, O. *et al.* Bioinspired interfacial engineering for highly stretchable electronics. *Nat. Commun.* **16**, 1337 (2025).

27. Haque, A. B. M. T. *et al.* Electrically Conductive Liquid Metal Composite Adhesives for Reversible Bonding of Soft Electronics. *Adv. Funct. Mater.* **34**, 2304101 (2024).

28. Tang, L., Wang, H., Ren, J. & Jiang, X. Highly robust soft-rigid connections via mechanical interlocking for assembling ultra-stretchable displays. *npj Flex. Elec.* **8**, 50 (2024).

29. Li, G. *et al.* Double-Sided Mechanical Interlocking Enables Soft-Rigid Conductive Interfaces With a Record High Toughness for Flexible Electronics. *Adv. Mater.* **38**, e73649 (2026).

30. Katayama, S. *et al.* Gas-permeable and stretchable nanoscale anisotropic conductive film for room-temperature, pressure-free interconnections. *Sci. Adv.* **12**, eaeh6203 (2026).

31. Zhao, Y. *et al.* A universal method for constructing stretchable and conductive connections in flexible electronics. *npj Flex. Elec.* **9**, 63 (2025).

32. Song, Y. *et al.* Stretchable and adhesive bilayers for electrical interfacing. *Mater. Horiz.* **12**, 1981–1991 (2025).

33. Zhu, T. *et al.* Topological Gradients for Metal Film-Based Strain Sensors. *Nano Lett.* **22**, 6637–6646 (2022).

34. Zhu, M. *et al.* A Mechanically Interlocking Strategy Based on Conductive Microbridges for Stretchable Electronics. *Adv. Mater.* **34**, 2101339 (2022).

35. Kang, J. *et al.* Tough and Water-Insensitive Self-Healing Elastomer for Robust Electronic

Skin. *Adv. Mater.* **30**, 1706846 (2018).

36. Chen, Q., Chen, M. & Qu, D. H. Dynamic Self-Healing Polymer Architectures for High-Performance Flexible Sensing. *Adv. Mater.* **38**, e73777 (2026).

37. Kim, S. M. *et al.* Superior Toughness and Fast Self-Healing at Room Temperature Engineered by Transparent Elastomers. *Adv. Mater.* **30**, 1705145 (2018).

38. Lee, Y. *et al.* Rapidly self-healing electronic skin for machine learning–assisted physiological and movement evaluation. *Sci. Adv.* **11**, eads1301 (2025).

39. Son, D. *et al.* An integrated self-healable electronic skin system fabricated via dynamic reconstruction of a nanostructured conducting network. *Nat. Nanotechnol.* **13**, 1057–1065 (2018).

40. Kim, K. *et al.* Assemblable thermoelectric Lego blocks for reconfigurable, self-healing, and flexible power generators. *npj Flex. Electron.* **10**, 30 (2026).

41. Jang, J. *et al.* Reconfigurable assembly of self-healing stretchable transistors and circuits for integrated systems. *Nat. Electron.* **8**, 474–484 (2025).

42. Choo, H. *et al.* Self-Healing and Stretchable Synaptic Transistor. *Adv. Funct. Mater.* **36**, e75662 (2026).

43. San, S. T. *et al.* Self-Soldering, Stretchable and Self-Healing Liquid Metal Elastomer Interconnections for Soft Electronics Platforms. *Adv. Mater. Technol.* **11**, e70992 (2026).

44. Pan, C. *et al.* Design strategies for liquid metal-based soft electronics. *Nat. Rev. Electr. Eng.;* 10.1038/s44287-026-00335-1 (2026).

45. Xiao, Y. *et al.* Liquid metal-based spatial-variant stretchable electronics via single-step programmable transfer printing. *Sci. Adv.* **12**, eaed4474 (2026).

46. Xu, Y. *et al.* Strain-resilient intrinsically stretchable electrochemical biointerfaces. *Science* **392**, eaed1630 (2026).

47. Li, J. *et al.* Strain-insensitive wet-tissue-adhesive biphasic bioelectronics for physicochemical monitoring and adaptive therapy. *Nat. Mater.* **25**, 1864–1872 (2026).

48. Wang, S. *et al.* Intrinsically stretchable electronics with ultrahigh deformability to monitor dynamically moving organs. *Sci. Adv.* **8**, eabl5511 (2022).

49. Jung, D. *et al.* Adaptive Self-Organization of Nanomaterials Enables Strain-Insensitive Resistance of Stretchable Metallic Nanocomposites. *Adv. Mat.* **34**, 2200980 (2022).

50. Sunwoo, S. H. *et al.* Stretchable Low-Impedance Nanocomposite Comprised of Ag–Au Core–Shell Nanowires and Pt Black for Epicardial Recording and Stimulation. *Adv. Mater. Technol.* **5**, 1900768 (2020).

51. Sunwoo, S. H. *et al.* Stretchable Low-Impedance Conductor with Ag–Au–Pt Core–Shell–Shell Nanowires and in Situ Formed Pt Nanoparticles for Wearable and Implantable Device. *ACS Nano* **17**, 7550–7561 (2023).

52. Li, X. *et al.* High-resolution liquid metal–based stretchable electronics enabled by colloidal self-assembly and microtransfer printing. *Sci. Adv.* **11**, eadw3044 (2025).

53. Baron, T. & Flachskampf, F. A. Simultaneous 4-Chamber Strain: More and Faster Analysis, but Is It Good Enough? *Circ. Cardiovasc. Imaging* **9**, e003895 (2016).

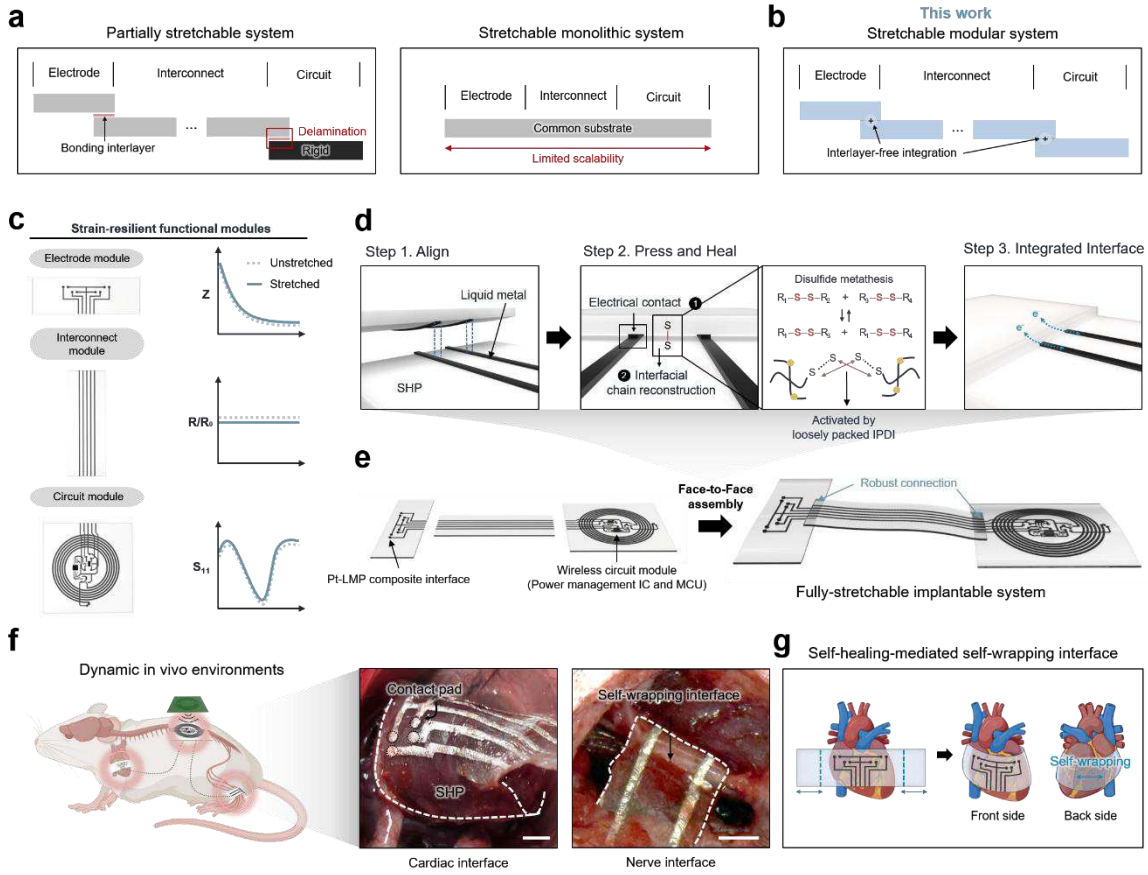


Fig. 1 | Overview of fully stretchable modular implantable bioelectronics

a Schematic comparison of partially stretchable system and fully-stretchable monolithic systems, highlighting interlayer-dependent junctions and limited scalability, respectively. **b** The proposed fully-stretchable modular system, in which electrode, interconnect and circuit modules are joined by interlayer-free integration. **c** Schematics of the three functional modules and their electrical responses before and after stretching: electrode impedance, interconnect resistance and circuit reflection coefficient (S_{11}). **d** Schematic illustration of module integration process. Alignment of pressing bring the liquid metal conductors into electrical contact, while interfacial chain reconstruction and disulfide metathesis join the self-healing polymer substrates. **e** Face-to-face assembly of each modules into a fully-stretchable implantable system. **f** Schematic illustration of the implantable system in a rat model and photographs showing its cardiac and nerve interfaces. Scale bar is 3 mm. **g** Schematic illustrations of the self-healing-mediated self-wrapping interface conforming to the heart.

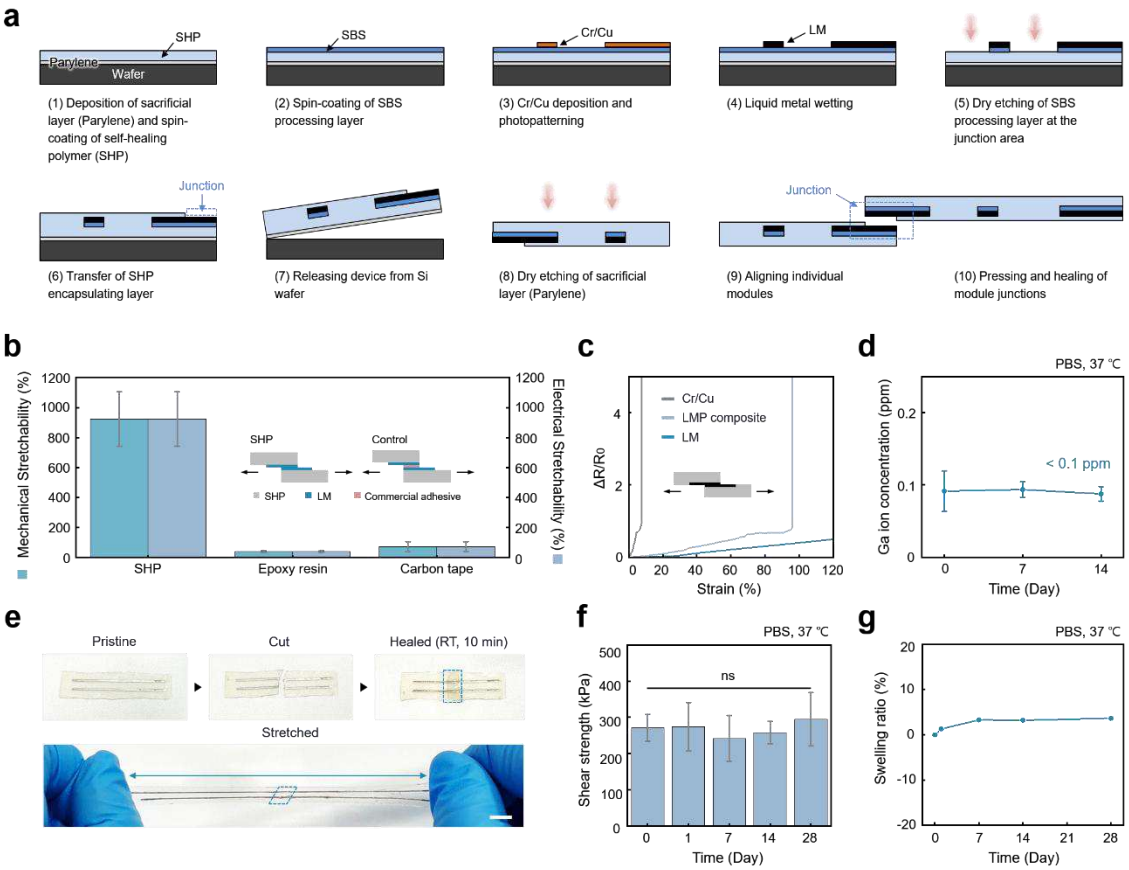


Fig. 2 | Self-healing-mediated interlayer-free integration of stretchable modules. **a** Schematics showing the fabrication process and interlayer-free integration strategies. **b** Comparison of the mechanical and electrical stretchability of SHP and commercial adhesives (overlapping area 10 mm width x 2 mm length; conductive trace 2 mm width). Error bars are standard deviation from 3 samples. **c** Relative resistance changes ($\Delta R/R_0$) under strain for Cr/Cu metal, liquid metal particle composite and liquid metal conductors (overlapping area 10 mm width x 2 mm length; conductive trace 2 mm width). **d** Gallium (Ga) ion concentrations in phosphate-buffered saline (PBS) during 14 days of immersion of the liquid metal device at 37 °C, determined by inductively coupled plasma mass spectrometry (ICP-MS). Error bars are standard deviation from 3 samples. **e** Photographs showing self-healing junction before cutting, after cutting and after healing for 10 min at room temperature, followed by stretching. Scale bar is 10 mm. **f** Shear strength of SHP junctions after immersion in PBS at 37 °C for 28 days; ns, not significant. (One-way ANOVA, $p = 0.842$, $n = 3$) **g** Swelling ratio over the same immersion period.

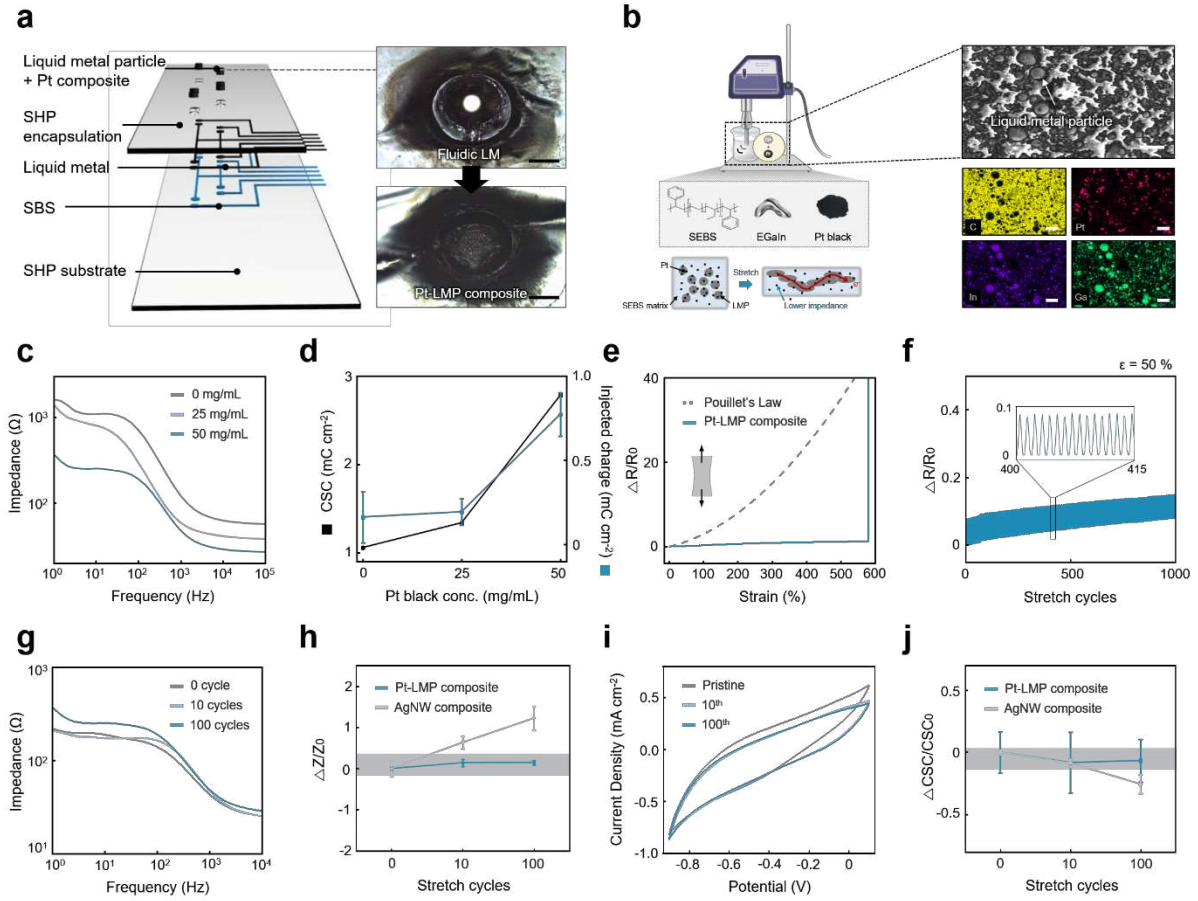


Fig. 3 | Structure and strain-resilient electrochemical performance of tissue-interfacing electrodes. a Exploded schematic of the electrode architecture, comprising Pt black-liquid metal particle (Pt-LMP) composite interface, liquid metal conductors. Optical images show a fluidic liquid metal electrode site before and after conductive encapsulation with the Pt-LMP composite. Scale bar is 500 μm. **b** Schematic of Pt-LMP composite preparation and its proposed operation under strain. LMP form connected conductive pathways during stretching, while Pt black lowers interfacial impedance. A scanning electron microscopy (SEM) image and corresponding energy-dispersive X-ray spectroscopy (EDS) elemental maps show the composite morphology and elemental distributions of carbon (C), platinum (Pt), indium (In) and gallium (Ga). Scale bar is 30 μm. **c** Impedance spectra of Pt-LMP composite containing 0, 25, 50 mg/mL of Pt black, measured from 100 to 105 Hz. **d** Charge storage capacity (CSC) and injected charge density as a function of Pt black concentration. Error bars are standard deviation from 3 samples. **e** Relative resistance changes ($\Delta R/R_0$) of the Pt-LMP composite under uniaxial tensile strain, compared with the response predicted by Pouillet's law. **f** Relative resistance changes of the Pt-LMP composite during 1,000 stretching cycles at 50% strain. Inset shows an enlarged segment of the cyclic response. **g** Impedance spectra of Pt-LMP composite before stretching and after 10, 100 stretching cycles, measured from 100 to 104 Hz. **h** Normalized impedance change ($\Delta Z/Z_0$) of Pt-LMP and AgNW composite electrodes after repeated stretching (0, 10, 100 cycles). Error bars are standard deviation from 3 samples. **i** Cyclic voltammetry profiles of the Pt-LMP electrode before stretching and after 10, 100 stretching cycles. **j** Relative CSC change ($\Delta CSC/CSC_0$) of Pt-LMP and AgNW composite electrodes after repeated stretching. Error bars are standard deviation from 3 samples.

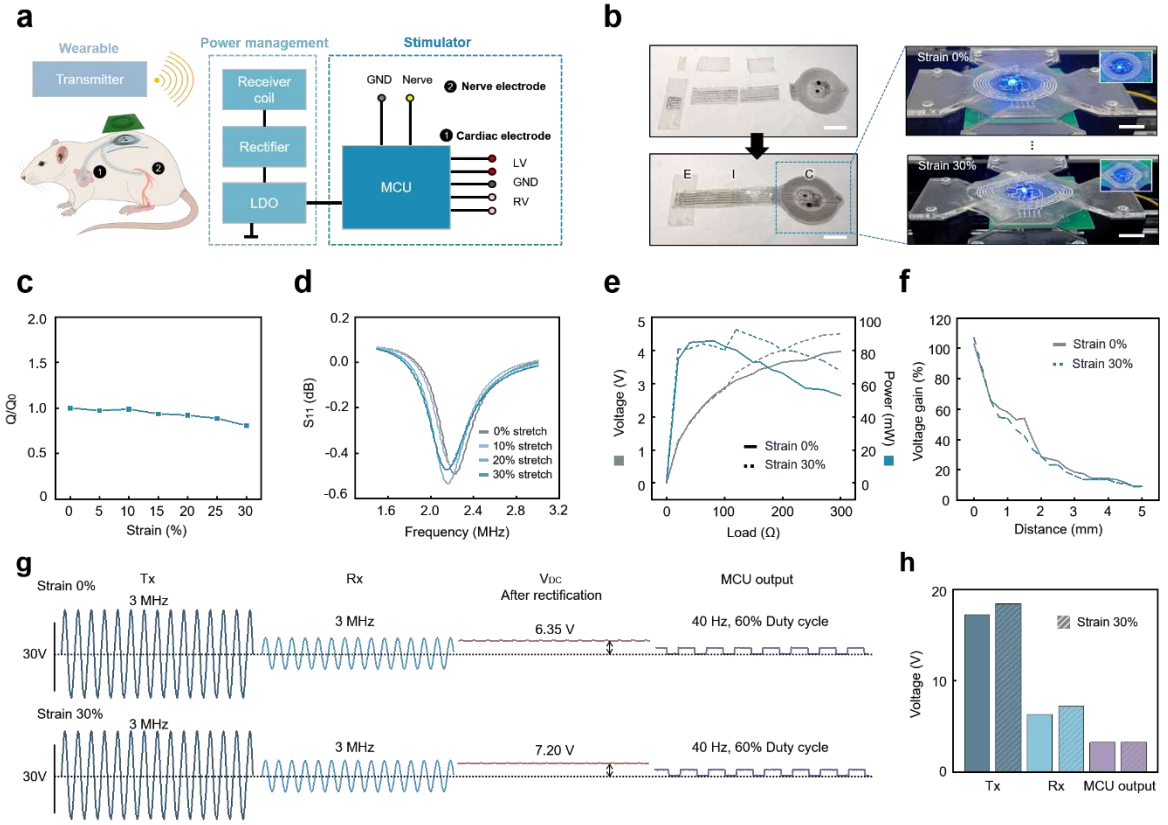


Fig. 4 | Strain-resilient electrical performance and wireless power transfer performance. **a** Functional block diagram of the wearable transmitter and implantable receiver, comprising the power management circuit and MCU-controlled stimulator. **b** Photographs of the individual modules and integrated device. The LED remains illuminated during wireless powering at both 0% and 30% strain. Scale bar is 20, 10 mm, respectively. **c** Normalized quality factor (Q/Q_0) of the receiver coil as a function of strain up to 30%. **d** Reflection coefficient (S11) of the LM-based receiver coil under strains ranging from 0% to 30%. **e** Rectified voltage and transferred power as functions of load resistance at 0% and 30% strain. **f** Voltage gain versus transmission distance (0-5 mm) at 0% and 30% strain. **g** Representative voltage waveforms at the transmitter (Tx), receiver (Rx), rectifier output (VDC), and MCU output at 0% and 30% strain. **h** Corresponding Tx, Rx, and MCU output voltages at 0% and 30% strain.

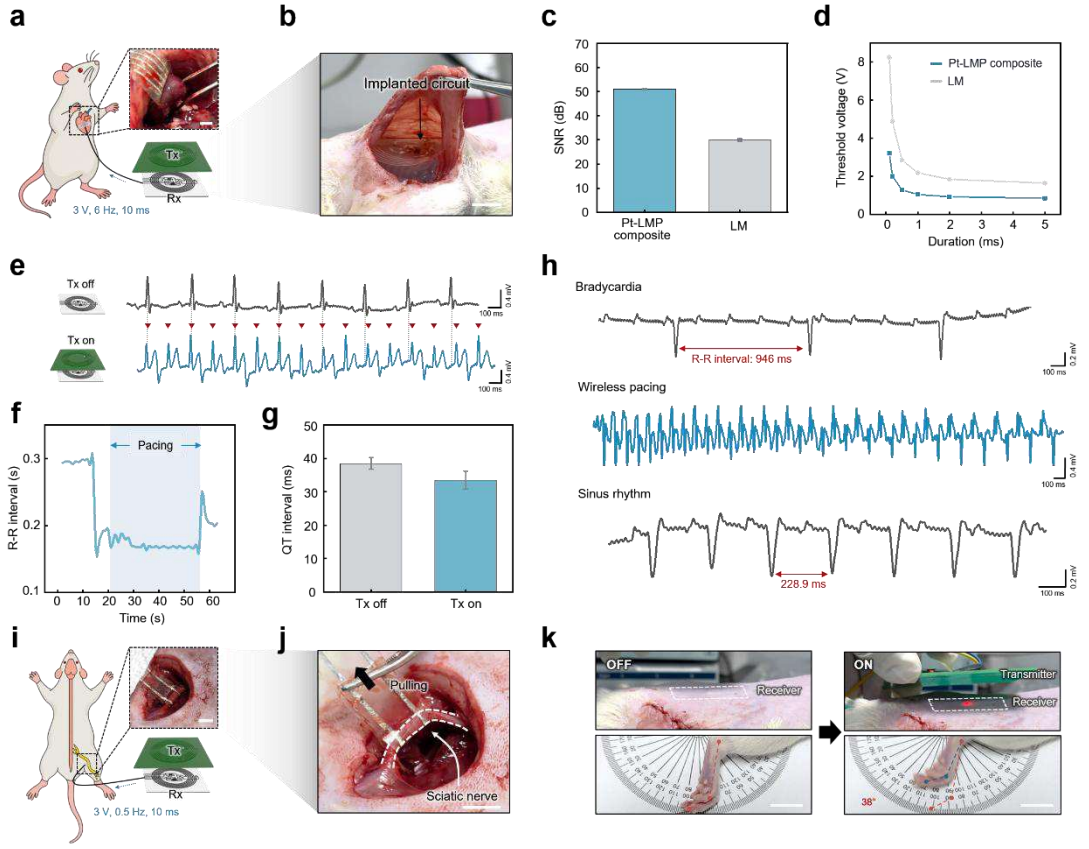


Fig. 5 | Wireless cardiac and peripheral nerve stimulation in rat models.
a Schematic of the cardiac interface and photograph of the electrode attached to the rat heart. Wireless stimulation was delivered at 3 V and 6 Hz with 10 ms pulse width. Scale bar is 5 mm. **b** Photograph of the implanted circuit module. Scale bar is 10 mm. **c** Signal-to-noise ratios (SNR) of epicardial electrograms recorded using Pt-LMP composite and LM electrodes. Error bars are standard deviation from 3 samples. **d** Strength–duration curves showing stimulation threshold voltage as a function of pulse duration. **e** Surface ECG recordings with the transmitter off and during 6 Hz wireless stimulation (on). **f** R–R intervals before, during and after 6 Hz wireless stimulation. **g** QT durations before, during and after 6 Hz wireless stimulation. Error bars are standard deviation from 3 samples. **h** Representative surface ECG recording during bradycardia, wireless pacing and subsequent sinus rhythm. **i** Schematic of the sciatic nerve interface and photograph of the electrode attached to the nerve. Wireless stimulation was delivered at 3 V and 0.5 Hz with 10 ms pulse width. Scale bar is 5 mm. **j** Photograph of the self-wrapped electrode around the sciatic nerve during gentle pulling. Scale bar is 5 mm. **k** Representative images of lower-limb movement with the transmitter off and on during wireless sciatic nerve stimulation at 3 V. Scale bar is 10 mm.

Supplementary Files

This is a list of supplementary files associated with this preprint. Click to download.

- 261007SIFigureNPJinvitation.pdf
- 261007SIvideoNPJinvitation.mp4